

Article

# The Role of Binders for Water-Based Anode Dispersions in Inkjet Printing

Cara Greta Kolb <sup>1,\*</sup> , Alessandro Sommer <sup>1</sup> , Maja Lehmann <sup>1</sup>, Carys-May Teixeira <sup>1</sup>, Hannes Panzer <sup>1</sup>, Saeed Maleksaeedi <sup>2</sup> and Michael Friedrich Zaeh <sup>1</sup>

<sup>1</sup> Department of Mechanical Engineering, TUM School of Engineering and Design, Institute for Machine Tools and Industrial Management, Technical University of Munich, Boltzmannstrasse 15, 85748 Garching, Germany; alessandro.sommer@iwb.tum.de (A.S.); maja.lehmann@iwb.tum.de (M.L.); carys-may.teixeira@tum.de (C.-M.T.); hannes.panzer@iwb.tum.de (H.P.); michael.zaeh@iwb.tum.de (M.F.Z.)

<sup>2</sup> Mechanical and Mechatronics Engineering, Multi-Scale Additive Manufacturing Lab, University of Waterloo, 295 Phillip St., Waterloo, ON N2L 3W8, Canada; saeed.maleksaeedi@uwaterloo.ca

\* Correspondence: cara.kolb@iwb.tum.de; Tel.: +49-89-289-15589

**Abstract:** Binders play a pivotal role in the production and the operation of lithium-ion batteries. They influence a number of key dispersion characteristics and battery parameters. In the light of growing interest in additive manufacturing technologies, binders were found to decisively govern the processability due to the induced complex non-Newtonian behavior. This paper examines the relevance of various binder derivatives for aqueous graphite dispersions that can be employed in inkjet printing. Two different carboxymethyl cellulose (CMC) derivatives with strongly deviating molecular weights were employed. The impact of the inherent polymer characteristics on the processability and the electrode characteristics were explored. Therefore, miscellaneous studies were carried out at the dispersion, the electrode, and the cell levels. The results revealed that the CMC with the lower molecular weight affected most of the studied characteristics more favorably than the counterpart with a higher molecular weight. In particular, the processability, encompassing drop formation and drop deposition, the cohesion behavior, and the electrochemical characteristics, were positively impacted by the low-molecular-weight CMC. The adhesion behavior was enhanced using the high-molecular-weight CMC. This demonstrates that the selection of a suitable binder derivative merits close attention.

**Keywords:** lithium-ion batteries; inkjet printing; electrode processing; water-based dispersions; binders



**Citation:** Kolb, C.G.; Sommer, A.; Lehmann, M.; Teixeira, C.-M.; Panzer, H.; Maleksaeedi, S.; Zaeh, M.F. The Role of Binders for Water-Based Anode Dispersions in Inkjet Printing. *Batteries* **2023**, *9*, 557. <https://doi.org/10.3390/batteries9110557>

Academic Editors: Yushi He, Carlos Ziebert and Zhong Ma

Received: 29 September 2023

Revised: 6 November 2023

Accepted: 9 November 2023

Published: 15 November 2023



**Copyright:** © 2023 by the authors. Licensee MDPI, Basel, Switzerland. This article is an open access article distributed under the terms and conditions of the Creative Commons Attribution (CC BY) license (<https://creativecommons.org/licenses/by/4.0/>).

## 1. Introduction

### 1.1. Motivation and Background

A sustainable energy future relies on substantial advances in electrochemical energy storage devices, such as supercapacitors and batteries [1,2]. While considerable progress has been made in harnessing novel promising materials [3], less attention has been paid to the development of capable electrode fabrication routes [4]. Conventionally, electrodes are generated by various techniques, which provide an efficient material deposition on an industrial scale [5]. Despite numerous advancements, these techniques have insurmountable restrictions in governing the geometry [6] and the structure of the electrodes [2]. Overcoming these restrictions is considered a key solution to realize higher material loadings without deteriorating the ion diffusion [2,7].

Novel approaches pursue the application of additive manufacturing techniques due to the unique geometrical design [2,8]. Liquid-based technologies are greatly appealing as they allow for the processing of electrode dispersions in a similar initial state as required for traditional processes [4,9]. Particular attention has been paid to piezoelectric inkjet printing [4], which, according to DIN EN ISO/ASTM 52900 [10], pertains to the material jetting category. In this process, a dispersion is ejected through a nozzle drop by drop

and deposited onto a substrate [11]. Due to the predefined overlap, drops merge into a homogeneous layer structure [11]. To achieve a high printing resolution and reproducibility, the dispersion needs to meet stringent specifications [12]. First, the dispersion is required to exhibit a long shelf life to mitigate the formation of agglomerates and sediments. These instability phenomena endanger nozzle clogging and bridging [13,14]. Second, the dispersion properties have to be adjusted to the print head qualities for a stable drop formation and drop deposition [11,15]. In this context of formulating suitable dispersions, binders play a key role despite their minor proportion of the total dispersion composition and their negligible chemical and electrochemical inactivity in the cell setup [16,17].

The core functions of binders are to ensure good cohesion between the particulate materials and a sufficient adhesion to the current collectors [17,18]. Additionally, they are paramount for the mechanical integrity of the electrode due to structural expansions and contractions during cycling [19,20]. However, most typical binders cause a complex non-Newtonian dispersion behavior. While this usually promotes the shelf life [21] and drop deposition [22], drop formation is substantially compromised [23,24]. For other dispersion systems, these effects were found to strongly depend on the content and the molecular weight of the employed binders [24,25], although the underlying phenomena are not yet fully understood [15,26]. However, this has not been explored for electrode dispersions despite binders of various molecular weight being employed in conventional lithium-ion battery production [17]. In the context of aqueous anode formulations, this particularly applies for CMC, which in combination with styrene-butadiene rubber (SBR) represents the most commonly employed state-of-the-art binder compound [17]. Pure CMC works as a thickening agent for graphite-based dispersions, which considerably promotes dispersion stability [17]. Additionally, it was reported to positively affect the electrochemical properties, such as charge transfer resistance and ionic conductivity [27,28], as well as the battery safety [29]. Although CMC is widely suggested as a promising binder, its stiffness, brittleness, and low elongation capacity pose challenges for large-scale applications [17]. Due to these drawbacks, the use of CMC can cause large cracks in the electrode surface and the coating is likely to be removed from the substrate during assembly and operation [30,31]. The addition of SBR can combat the disadvantages accredited to pure CMC and thus results in improved dispersion and electrode characteristics, such as adequate wetting, less brittleness, higher flexibility, and stronger adhesion to the current collector foils [32,33]. Apart from the printing conditions, little attention has been directed to the impact of binder derivatives on the performance characteristics of lithium-ion batteries.

### *1.2. Approach*

This paper explores the role of binder derivatives for water-based graphite dispersions formulated for application in inkjet printing. We used a dispersion composition as a reference whose processability we have already demonstrated [34]. Following this procedure, two different CMC derivatives with strongly varying molecular weights were employed. They are referred to as low-molecular-weight (l-mw) and high-molecular-weight (h-mw) CMC. The effects of the intrinsic polymer characteristics on processability and electrochemical performance were explored. Various studies were conducted at the dispersion, the electrode, and the cell levels. At the dispersion level, the rheological behavior was characterized to gain insight into stability and printability behavior. Drop formation and drop deposition were evaluated in an in situ and ex situ test setup, respectively. The dispersion samples were used to fabricate electrode coatings to further analyze the mechanical properties. Finally, the electrode samples were subjected to an electrochemical testing at the cell level. The material behavior was also compared against conventionally fabricated electrode samples.

## 2. Materials and Methods

### 2.1. Materials

**Preparation of the dispersions.** The dispersion samples were prepared according to the procedure outlined in Kolb et al. [34]. The sample composition and the specification of the constituents are provided in Table 1.

**Table 1.** Composition of the graphite dispersions; the contents marked with a (\*) refer to the amount of the active material employed.

Component	Material	Supplier Specification	Content in m%
Active material	Graphite	NG08BE0305, Nanografi, Turkey	2
Dispersant	PVP	Luvitec K17, BASF, Germany	15 *
Binder 1	CMC	l-mw: 419273, Merck, Germany	2, 3, 4, 5, 6, 7, and 8 *
		h-mw: Sunrose, Nippon Paper Industries, Japan	2, 3, 4, 5, 6, 7, and 8 *
Binder 2	SBR	SBR, Zeon Corporation, Japan	5 *

Polyvinylpyrrolidone (PVP) was used as a dispersant as we have demonstrated its effectiveness to stabilize graphite in aqueous media in various publications (see, e.g., [35,36]). A co-binder system was employed, encompassing both CMC and SBR. This allows for an alignment with recent findings on conventional water-based fabrication routes [17]. The polymer-specific characteristics of the l-mw and the h-mw CMC are summarized in Table 2. In addition to the molecular weight, the degree of substitution (DS) significantly impacts the solubility of the CMC in water [37]. The DS of a polymer is defined as the number of substituents that are bound per base unit [38]. To maintain comparability, the DS of the l-mw and the h-mw CMC was selected within the same range proposed by Lee et al. [39] and Wuestenberg [37] to achieve a superior dispersion stability. The molecular weight was varied by a factor of two, as other research groups have demonstrated that this difference yields significant results (see e.g., Ishii and Nakamura [40]). The terminology used throughout this paper to specify the respective samples is as follows: xl-mw and yh-mw represent dispersion samples with a content of x% l-mw CMC or y% h-mw CMC, respectively. The content refers to the amount of active material employed.

**Table 2.** Polymer-specific characteristics of the employed CMC derivatives.

Type	Degree of Substitution DS	Molecular Weight Mw in $\text{g mol}^{-1}$
l-mw	0.70	$9.0 \times 10^4$
h-mw	0.94	$1.8 \times 10^5$

Following the findings of Kolb et al. [34], drop formation was examined using samples with an altered surface tension. Therefore, a minimal quantity of the surfactant ethoxylated acetylenic diols (Surfynol 440, Evonik, Essen (Germany)) was added to adjust the surface tension in the target range between 35 and 40  $\text{mN m}^{-1}$  [41]. The modified samples are referred to as l-mw\* and h-mw\*. The remaining studies were conducted with the unmodified surface tension samples to maintain compatibility with previous studies. This appears to be a reasonable and conservative approach, since no distinct impact on the rheological properties is to be expected and drop deposition behaves more poorly without modification.

**Electrode fabrication.** A tape casting coater (MSK-AFA-III, MTI, Richmond (VA, USA)) was used to coat the dispersions onto the copper current collector foils (Cu-PHC, Schlenk, Barnsdorf (Germany)) with a thickness of 11  $\mu\text{m}$ . A doctor blade with a gap width of 250  $\mu\text{m}$  was employed. The as-prepared coating samples were dried at 60  $^{\circ}\text{C}$  in a convection oven (Mehrzweck-Heissluftofen, Bartscher, Salzkotten (Germany)).

**Cell assembly.** Half-cells (CR2032, Hohsen, Tokyo (Japan)) were assembled from the electrode coatings. Therefore, electrode samples with a diameter of 15 mm were cut out of

the as-prepared coating samples using a handheld punch (00565, Nogami, Hitachiomiya City (Japan)). The electrodes and the separators were dried in a vacuum oven (B-585, Büchi, Flawil (Switzerland)) at 60 °C under a vacuum of approx. 50 mbar for 12 h to remove residual moisture. All half-cells were assembled in a drying room with a dew point of −60 °C. For each half-cell, a sealing ring, a metal spacer (thickness: 0.5 mm), the lithium foil (diameter: 14 mm, thickness: 250 µm) (PI-KEM, Wilnecote (UK)) two glass fiber separators (diameter: 16 mm) (Type 691, VWR, Radnor (PA, USA)), the graphite electrode, another spacer (thickness: 1.0 mm), and a contact spring were stacked centered in the cell housing. Each of the coin cells was filled with 110 µL of electrolyte (LP572, BASF, Ludwigshafen (Germany)) which consists of 1 mol lithium hexafluorophosphate (LiPF<sub>6</sub>) conducting salt in a 3:7 mass ratio of ethylene carbonate (EC) and ethyl methyl carbonate (EMC) with 2 m% vinylene carbonate (VC).

**Preparation of the reference electrodes.** The graphite (SMG-A5, Hitachi Chemical, Tokyo (Japan)) was dry mixed with carbon black (C-Nergy Super C65, Imerys, Paris (France)) in a centrifugal mixer (Speedmixer DAC 1100.2 VAC-P, Hauschild, Hamm (Germany)) at 1400 rpm for 1 min. Concurrently, the binder solution consisting of distilled water and CMC (CMC, Sigma Aldrich, Darmstadt (Germany)) was blended using a disperser (Dispermat FM 10, VMA-Getzmann, Reichshof (Germany)) at 200 rpm with a tangential velocity of 10.47 m s<sup>−1</sup> for 40 min. The as-prepared dry mixture was added and dispersed for another 45 min at 2000 rpm. SBR (SBR BM-451-B, Zeon, Tokyo (Japan)) was added and the dispersion was mixed for 20 min at 500 rpm with a tangential velocity of 2.62 m s<sup>−1</sup>. Lastly, the as-prepared dispersion was degassed in a centrifugal gas mixer at 600 rpm and 250 mbar for 5 min, resulting in the final dispersion composition containing 94 m% graphite, 1.0 m% conductive carbon, 2.0 m% CMC, and 3.0 m% SBR.

An industrial roll-to-roll coating machine (BC50, Coatema GmbH, Dormagen (Germany)) equipped with an infrared dryer was employed to doctor-blade coat the reference electrode dispersions onto the copper current collector foils (Cu-PHC, Schlenk, Barnsdorf (Germany)) with a thickness of 10 µm. The gap width was 96 µm and the coating speed was adjusted to 1 m min<sup>−1</sup>. A total coating loading of 9.79 mg cm<sup>−3</sup> was obtained, which correlated to an active material loading of 9.2 mg cm<sup>−3</sup>. The coatings were compressed to a porosity of approx. 30% using a calender (EA 102, Coatema, Dormagen (Germany)) with a maximum line load of 1000 N mm<sup>−2</sup> and a roller diameter of 400 mm. The roller speed was set to 1 m min<sup>−1</sup>.

## 2.2. Characterization

This section outlines the characterization methods employed and the associated parameters at the respective levels of the analysis.

### 2.2.1. Dispersions

**Rheological behavior.** The rheological behavior of the dispersion samples was determined using a rotational rheometer (Kinexus lab+, Netzsch, Selb (Germany)), which was equipped with a passive solvent trap. A 40 mm plate–plate geometry was employed, whose gap distance was adjusted to 0.1 mm. Each measurement was conducted at ambient temperature after an equilibration of 5 min. Shear rate sweeps were performed to examine the shear-dependent flow behavior and the viscosity at drop ejection  $\eta_{\text{eject}}$ . Therefore, the viscosity was measured as a function of the shear rate from 10<sup>0</sup> to the limit of the measuring range 10<sup>4</sup> s<sup>−1</sup>. Considering that the shear rate at drop ejection  $\dot{\gamma}_{\text{eject}}$  is of the order of 10<sup>5</sup> to 10<sup>6</sup> s<sup>−1</sup> for the print head system [34] used, the empirically obtained viscosity values were extrapolated by applying a fluid dynamic model. Depending on the sample-specific properties, either the power law or the Herschel–Bulkley model was employed. While the power law model can be described as [42]

$$\tau = k \times \dot{\gamma}_{\text{eject}}^n \quad (1)$$

the Herschel–Bulkley model is defined as [43]

$$\tau = \tau_{\text{HB}} + k \times \dot{\gamma}_{\text{eject}}^n \quad (2)$$

where  $k$  is the consistency index,  $n$  the index, and  $\tau_{\text{HB}}$  the flow point. For each dispersion sample, the model type that yielded the higher adjusted coefficient of determination  $R_{\text{adj}}^2$  was applied.

Amplitude tests were conducted to determine the yield point and thus the linear viscoelastic (LVE) range of the dispersion samples. The storage modulus  $G'$  and the loss modulus  $G''$  were examined over a shear strain in a range between  $10^{-2}$  and  $10^2\%$ . Frequency tests were performed based on the amplitude tests to characterize the material behavior and the expected stability. In addition, the relaxation time  $\lambda$  was derived.  $G'$  and  $G''$  were measured within a frequency range between  $10^{-1}$  and  $10^2$  Hz.

**Surface tension.** The surface tension of the dispersion samples was examined according to the stalagmometric method reported by Traube [44]. For each dispersion sample, the average weight was determined based on ten drops. Deionized water was used as a calibration medium. Three measurements were performed per sample.

### 2.2.2. Electrodes

**Adhesion and cohesion behavior.** The adhesion and cohesion behavior of the electrode samples were analyzed using a universal tensile test machine (ProLine Z050, ZwickRoell, Ulm (Germany)) with an integrated load cell possessing a maximum nominal force of 1 kN (Xforce HP, ZwickRoell, Ulm (Germany)). The pull-off tests followed the test procedure proposed by Haselrieder et al. [45]. The electrode samples were fixed to the bottom testing area with double-sided adhesive tape. The upper testing area was also equipped with a double-sided adhesive tape. Both the electrode samples and the adhesive tape were cut to form a 9 mm wad punch (W572, FORMAT, Wuppertal (Germany)), while the testing area on the sample holders exhibited a diameter of 8 mm. The electrode samples were subjected to a compression phase and a dwell phase to allow for a proper contact between the tapes and the electrodes before the pull-off testing. Therefore, the upper sample holder was lowered at  $0.75 \text{ mm min}^{-1}$ , followed by a compression period of 30 s and a pull-off at a defined velocity of  $100 \text{ mm min}^{-1}$ . The maximum adhesion force  $F_n$  and the compression force  $F_c$  required for a clean pull-off were determined with an integrated software program (TestExpertIII, ZwickRoell, Ulm (Germany)) and converted to the respective stresses  $\sigma_n$  and  $\sigma_c$ . A sample cross-section of  $50.27 \text{ mm}^2$  was considered for the calculations. The total adhesion strength  $\sigma_{\text{total}}$  was determined as a sum of  $\sigma_n$  and  $\sigma_c$ . Three samples of each electrode composition were analyzed. The cohesion behavior was derived from the present failure mechanism.

### 2.2.3. Cells

**Formation and rate capability tests.** The formation was performed at a constant ambient temperature of  $25 \text{ }^\circ\text{C}$  using a battery cell test system (CTS, BaSyTec, Asselfingen (Germany)). The half-cell samples underwent a total of three charge and discharge cycles by applying a constant current of 0.1 C within a voltage range of 0.01 and 1.5 V. After each charge or discharge, the galvanostatic cycling was paused for 20 min. The C-rates employed throughout the formation were determined with the theoretical capacities, which were calculated on the basis of the active material loading and the specific active material capacity. The weight of the anodes was determined with a precision balance with an accuracy of 0.001 mg (AX26, Mettler Toledo, Columbus (OH, USA)). The conventionally produced half-cells with known electrochemical behavior served for the validation of the testing procedure. Each standard deviation was derived from three half-cell samples.

### 2.3. Drop Monitoring

#### 2.3.1. Drop Formation

The test setup described in Lehmann et al. [46] was utilized for the monitoring of the drop formation. The drops were generated by a piezoelectric print head (Spectra SL-128 AA, Fujifilm, Tokyo (Japan)) with a nozzle diameter of 50  $\mu\text{m}$ . The print head was installed within a binder jetting setup (VTS128, Voxeljet Technology GmbH, Friedberg (Germany)) that is also capable of inkjet printing. The piezoelectric print head operated with a voltage of 80 V and a pulse frequency of 1000 Hz. The number of observable drops was adjusted to 5000.

The drop formation imagery was recorded with a high-speed camera (iSpeed, Olympus, Tokyo (Japan)) that was equipped with a Sigma objective lens with a 105 mm focal length and 68 mm long extension rings. A high-power LED (M405LP1, Thorlabs, Inc., Newton (MA, USA)) was focused behind the print head with a collimator (SM2P50-A, Thorlabs, Inc., Newton (MA, USA)) and controlled by an LED driver (LEDD1B T-Cube, Thorlabs, Inc., Newton (MA, USA)). The parameters for drop formation recordings are given in Table 3.

**Table 3.** Parameter setting employed for drop formation recording.

Characteristics	Value
Aperture	$f/2.8$
Exposure	2.16 $\mu\text{s}$
Frame rate	2000–20,000 fps

#### 2.3.2. Drop Deposition

The contact angle  $\theta$  of the dispersion samples was measured according to the sessile drop method using a drop shape analyzer (DSA25E, Krüss Scientific, Hamburg (Germany)) with an integrated camera. The drops were generated by a standardized syringe with a tip diameter of 0.5 mm and deposited onto a copper foil that was attached to a glass plate. Throughout the analyses, the drop rate was held constant at a value of 4  $\mu\text{L/s}$ . To determine the dynamic contact angle, each drop was recorded for 60 s post the initial impact. An image was extracted every 10 s and the contact angle was determined using the software *ImageJ 1.53t*. The standard deviation was calculated from three dispersion samples.

## 3. Results and Discussion

For clarity, only selected binder curves are presented for the respective studies.

### 3.1. Processability

#### 3.1.1. Stability

**Determination of the LVE region.** The LVE region describes the range in which the dispersion sample is not irretrievably degraded due to the applied shear strain [42,47]. This range was extracted from the obtained amplitude test data for the storage modulus  $G'$  and the loss modulus  $G''$ .  $G'$  quantifies the deformation energy that can be stored within the dispersion sample while subjected to a shear stress, which reflects the elastic behavior [42]. In contrast,  $G''$  can be understood as a measure for the deformation energy that is expended during the structural changes of the dispersion sample under the influence of a shear stress, which correlates to the viscous behavior [42]. In this light, the LVE region is characterized by the quasi-constant plateau values for both  $G'$  and  $G''$  when plotted in a double logarithmic diagram [47]. The shear rate at which  $G'$  begins to decline marks the limit of the LVE region. The LVE region data obtained for the l-mw and h-mw dispersion samples are summarized in Table 4.

The values for the LVE region indicate that there is no clear dependence on the molecular weight and the binder content. This can be attributed to the high standard deviations that usually underlie amplitude tests. To assure a non-destructive deformation

in the frequency sweep, the shear-strain amplitude must be within the LVE region. To maintain consistency throughout all dispersion samples, a shear-strain amplitude valid for all dispersion samples was pursued. Accordingly, a shear-strain amplitude of 0.1% was identified, as this value lies within the particular LVE regions. This concurs with the studies of Barnes [47], who also pinpointed a shear-strain amplitude of 0.1% as appropriate to analyze dispersion samples in the frequency sweeps.

**Table 4.** Values of the empirically determined LVE regions for the l-mw and h-mw dispersion samples.

Binder Content in m%	l-mw in %	h-mw in %
2	0.01–7.94	0.01–2
3	0.01–7.95	0.01–0.102
4	0.01–0.198	0.01–0.796
5	0.01–0.795	0.01–10
6	0.01–1.26	0.01–12.6
7	0.01–2	0.01–1
8	0.01–2	0.01–100

**Analysis of the material behavior.** Frequency tests provide insight into the time-dependent deformation behavior of a dispersion sample [42,47]. The short-term behavior can be imitated by high frequencies, while the long-term behavior is simulated by applying low frequencies [47]. Frequency regions which exhibit  $G'$  curves with predominantly larger values than those of the  $G''$  curves indicate an elastic behavior, while the opposite substantiates a dominant viscous behavior [42,47]. Accordingly, the frequency-dependent material behavior of the dispersion samples was characterized based on an analysis of the curve progressions. The evaluation yielded the results condensed in Table 5.

**Table 5.** Overview of the frequency-dependent material behavior of the l-mw and h-mw dispersion samples; the frequency ranges are classified as follows:  $10^{-1}$  Hz  $< f_{low} \leq 5 \times 10^{-1}$  Hz and  $5 \times 10^{-1}$  Hz  $< f_{high} \leq 10^2$  Hz.

Sample	$f_{low}$	$f_{high}$	Sample	$f_{low}$	$f_{high}$
2l-mw	$G' > G''$	$G' > G''$	2h-mw	$G' > G''$	$G' > G''$
3l-mw	$G' > G''$	$G' > G''$	3h-mw	$G' > G''$	$G' > G''$
4l-mw	$G' > G''$	$G' > G''$	4h-mw	$G' > G''$	$G' > G''$
5l-mw	$G' > G''$	$G' > G''$	5h-mw	$G' > G''$	$G' > G''$
6l-mw	$G' > G''$	$G' > G''$	6h-mw	$G' > G''$	$G' > G''$
7l-mw	$G' > G''$	$G' > G''$	7h-mw	$G' > G''$	$G'' > G'$
8l-mw	$G'' > G'$	$G' > G''$	8h-mw	$G' > G''$	$G'' > G'$

It follows from Table 5 that the majority of the analyzed dispersion samples exhibit a rather elastic behavior for both the low and high frequency regions. This indicates that the dispersion samples are able to restore their initial state partially or fully throughout the observed frequency range [42,47]. Consequently, these dispersion samples exhibit an appropriate stability [48]. For higher binder contents, a shift in the material can be recognized for both the l-mw and h-mw dispersion samples. While the 8l-mw dispersion sample exhibits a viscous long-term behavior, the 7h-mw and the 8h-mw dispersion samples show a viscous short-term behavior.

This indicates that the oscillatory regions distinguishable for the polymer systems depend on the molecular weight and the content of the employed polymer, as observed by Barnes [47] and Mezger [49]. The dominance of the  $G''$  values at lower frequencies for the 8l-mw dispersion samples can likely be accredited to more prominent friction forces. Chain entanglements begin to develop if the polymer content is high enough. These entanglements become more rigid and inflexible as the frequency is increased. This is associated with an increased storage of deformation energy and thus a dominant elastic

behavior. The characteristic prevailing of  $G''$  over  $G'$  at high frequencies was also reported by Barnes [47] for polymers with higher molecular weights, such as polydimethylsiloxane, polystyrene, and poly(methyl methacrylate). Accordingly, the stability behavior of the h-mw dispersion samples is slightly more distinct.

### 3.1.2. Printability

**Flow behavior.** Figure 1 provides the course of the viscosity over the shear rate for selective l-mw and h-mw dispersion samples. The extrapolation of the measured data according to the power law or Herschel–Bulkley model is also visualized in the graphs. The close-ups elucidate the flow behavior at shear rates approaching the measuring limit.

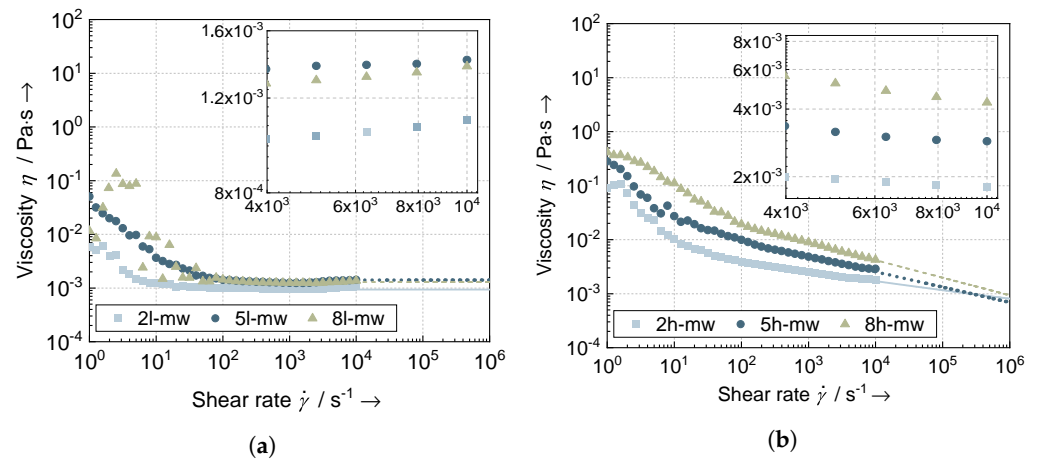


**Figure 1.** Viscosity  $\eta$  as a function of the shear rate  $\dot{\gamma}$  for the (a) l-mw and (b) h-mw dispersion samples; the measured data were extrapolated by applying the power law or Herschel–Bulkley model (see Table 6).

**Table 6.** Overview of the determined parameters of the power law or Herschel–Bulkley equation for the different dispersion samples

Type	Binder Content	Consistency Index $k$	Index $n$	Flow Point $\tau_{HB}$	Adjusted $R^2_{adj}$
-	in m%	-	-	-	-
l-mw	2.0	$5.68 \times 10^{-3}$	-1.05	$9.37 \times 10^{-4}$	0.927
	5.0	$45.63 \times 10^{-3}$	-1.16	$14.03 \times 10^{-4}$	0.989
	8.0	$8.34 \times 10^{-3}$	-2.13	$12.90 \times 10^{-4}$	0.674
h-mw	2.0	$9.00 \times 10^{-3}$	-0.19	$1.77 \times 10^{-4}$	0.996
	5.0	$34.55 \times 10^{-3}$	-0.28	-	0.976
	8.0	$83.48 \times 10^{-3}$	-0.33	-	0.998

The l-mw dispersion samples show the same characteristic trend for each composition. At low shear rates, the dispersion samples exhibit comparatively high viscosity values. With an increasing shear rate, the viscosity curves decrease until a quasi-constant value is reached. The gradient appears to increase with a rising binder content, although the 8l-mw dispersion sample is subject to strong variations. This indicates a shear-thinning behavior, whereby the effect is more pronounced at higher binder contents. Towards the limit of the measuring range, a slight decrease in the viscosity values and thus a shear-thickening behavior can be observed in the close-up (see Figure 1a). The h-mw dispersion samples show a similar trend (see Figure 1b), although the shear-thinning behavior is more distinct with higher initial viscosity values and lower extrapolated viscosity values. Additionally, the viscosity values do not reach a constant limit.

These phenomena can be attributed to the polymer–particle network that is formed between the binder molecules and the graphite particles [50,51]. More specifically, the

interactions occur between the CMC backbone and the hydrophobic graphite particles [17]. The relatively high viscosity values at low shear rates indicate that both the l-mw and the h-mw CMC form a viable polymer–particle network with the graphite particles during the synthesis process. The longer backbone of the h-mw CMC provides more functional groups that can interact among each other and the graphite particles, yielding a stronger and likely larger-scale network. This is also reflected in the higher deviation of the viscosity values for the 8l-mw dispersion sample. The surplus in polymer molecules cannot be entirely incorporated in the forming network, leading to steric hindrances in the solution. At higher shear rates, the network structure is progressively destroyed. The prevalent shear forces cause the particles to realign themselves in a comparably ordered structure that lies parallel to the applied shear field [9]. The binder molecules and particles are no longer or only weakly bound to one another, which allows them to slide past each other more freely [9]. The reaching of constant viscosity values for the l-mw dispersion samples indicates the complete demolition of the initial polymer–particle network. Due to the absence of interactions between the polymers and the particles, the viscosity values approach a Newtonian limit that cannot be exceeded. In contrast, the h-mw CMC offers more connecting points for potential interactions that require even higher shear stresses to be overcome. The slight shear-thickening behavior of the l-mw samples can be also explained by the destruction of the polymer–particle network, which leaves the particles exposed to substantially more particle collisions. This creates friction, which causes an increase in the overall viscosity [52,53]. In this context, Ishii and Nakamura [40] further assumed that the CMC acts as a buffer layer and suppressor for the presence of shear-thickening behavior as long as it is adsorbed onto the graphite particle surface.

### 3.2. Drop Monitoring

#### 3.2.1. Drop Formation

According to Wijshoff [11], a stable drop formation refers to the printing condition in which a single drop is generated in the absence of extra drops. In contrast, the appearance of these *satellite drops* is indicative of an inadequate printing regime [54].

The drop formations of the viably processable l-mw\* and h-mw\* dispersion samples are displayed in Figure 2. The captured images show the process throughout the filament ejection, the thinning, and the detachment to the formation of the drop. The black lining visible at the top of the images represents the cross-section of the print head.

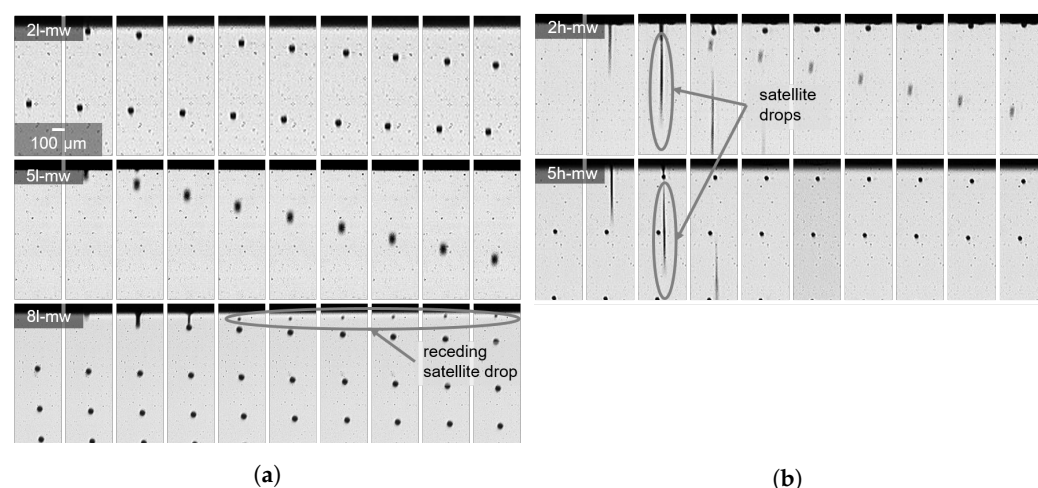


**Figure 2.** Drop monitoring images of the (a) l-mw\* and (b) h-mw\* dispersion samples; the time interval between two consecutive frames was 50  $\mu$ s.

The l-mw\* dispersion samples could be processed, although only the 2l-mw\* and the 5l-mw\* dispersion samples showed a stable drop formation. The 8l-mw\* sample exhibited a receding satellite drop. For the h-mw\* dispersion samples, only the 2h-mw\* and the 5h-mw\* dispersion samples allowed for processing, but in an unstable regime.

The respective flight paths of the initial drops were characterized by numerous satellite drops. Consequently, the original drops were not deposited in an accurate and reproducible pattern which compromises the printing resolution.

These findings concur with the studies of Xu et al. [23] and Morrison and Harlen [55]. They found that drop formation behavior strongly depends on the content and the molecular weight of the employed binder. The progression of the l-mw\* dispersion samples agrees well with the findings that drop formation is inhibited at a higher binder content. This was also noted for the h-mw\* dispersion samples, although no stable regime was observed in between the instable processing and the viscous dissipation. Hoath [50] offered an explanation for the different behavior of the l-mw\* and the h-mw\* dispersion samples. Accordingly, the restricting and inhibiting factor for printing is the extensibility of the polymer chains at higher molecular weights. The rigid rod orientation affects a more distinct jamming that limits the maximum possible printable polymer content. These investigations demonstrate that the l-mw CMC facilitates drop formation and allows for a stable processing within a certain parameter window.

### 3.2.2. Drop Deposition

Figure 3 displays the course of the contact angle  $\theta$  over the wetting time  $t$  for the l-mw and h-mw dispersion samples. While the average contact angle values range from 69 to 89° for the l-mw dispersion samples, they lie between 79 and 96° for the h-mw dispersion samples. Accordingly, the h-mw dispersion samples exhibit overall larger values than their l-mw counterparts. In addition, it is discernible that the contact angle values decrease over time for all investigated dispersion samples. No clear dependence can be recognized regarding the influence of the binder content among each binder system. This is ascribed to the large standard deviations that are typical for contact angle measurements. They stem from the distinct inaccuracies that arise from the positioning of the substrate, variations in the surface roughness [56,57], and the analysis based on a manual setting of the tangent line [58,59].

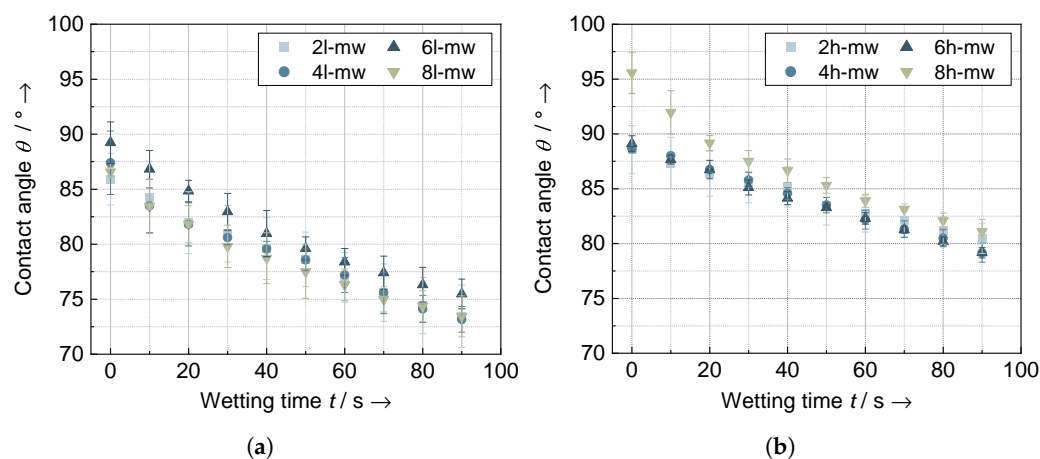


**Figure 3.** Contact angle  $\theta$  between the dispersion and the copper foil as a function of the wetting time  $t$  for selected (a) l-mw and (b) h-mw dispersion samples

These observations can possibly be explained by the coiling effects of the polymers [50]. Accordingly, the compounds strive to restore their stable coil configuration upon ejection. Intuitively, h-mw polymers are prone to form more extensive coil bundles than l-mw polymers. The differences can thus be attributed to the following phenomena. On the one hand, the restoration of the stable coil configuration within drop may take longer for the h-mw dispersion samples than for their l-mw counterparts. This explains the different contact angles at the same time stamps and, in addition to the solvent evaporation, causes the temporal decrease of the contact angle values. On the other hand, the extent of the polymer bundles and their interactions among each other, the solvent, and the particulate phase is stronger within the l-mw dispersion samples. This indicates that the drop adheres to itself more prominently

than to the substrate. Billot et al. [60] stated that a sufficient wetting can be expected for contact angle values below  $90^\circ$ . Hence, an adequate wetting can be assumed for the l-mw dispersion samples and the majority of the h-mw dispersion samples.

### 3.3. Electrode Characteristics

#### 3.3.1. Adhesion and Cohesion Behavior

Figure 4 displays the strength values of the l-mw and h-mw electrode samples. The samples that are not represented did not exhibit a clean pull-off.

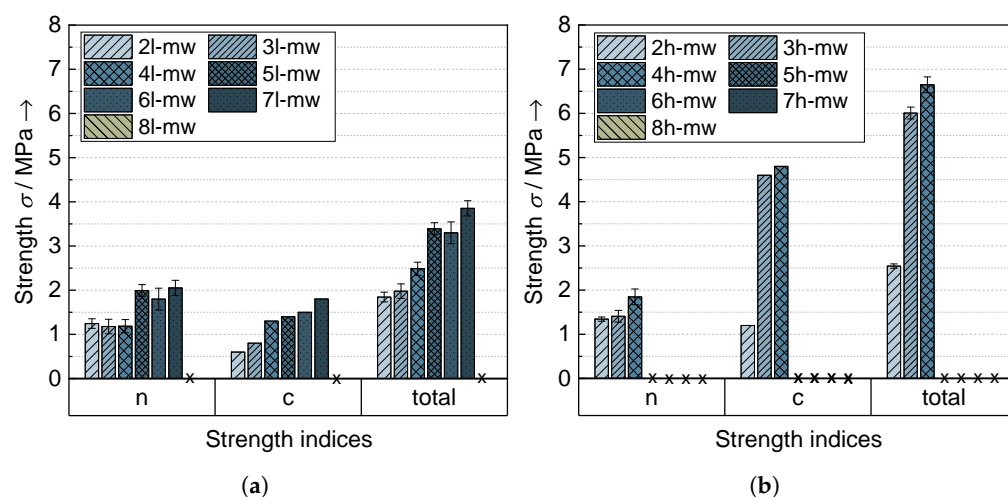


**Figure 4.** Adhesion strength values for the (a) l-mw and (b) h-mw electrode samples.  $\sigma_n$  represents the adhesion strength,  $\sigma_c$  the maximum compression strength, and  $\sigma_{total}$  the sum of  $\sigma_n$  and  $\sigma_c$ ; the 'x' indicates that for the given samples no clean pull-off could be achieved.

For the l-mw electrode samples, no clear correlation appears for  $\sigma_n$ . The  $\sigma_c$  values show a more indicative relationship, such that the compression strength rises slightly with an increasing binder content. The  $\sigma_{total}$  values exhibit a more pronounced trend towards higher values with an increasing binder content. The 6l-mw dispersion sample marks a minor deviation in this trend, which is likely a measuring inaccuracy. A similar behavior can be observed for the h-mw electrode samples, although the correlations between  $\sigma_n$ ,  $\sigma_c$ , and  $\sigma_{total}$  and the binder content are more distinct. Additionally,  $\sigma_c$  and  $\sigma_{total}$  show a rapid increase from the 2h-mw to the 3h-mw electrode sample. The comparative analysis reveals that the values for  $\sigma_n$  and  $\sigma_c$  are significantly higher for the h-mw electrode samples than for their l-mw counterparts. Furthermore, it is obvious that the h-mw electrode samples do not allow for a clean pull-off already at lower binder contents. For these electrode samples, a cohesion failure prevailed over a failure in the adhesion interphase. This indicates that for the h-mw electrode samples cohesion failures occur more prominently.

These peculiarities concur with the observations of Liu et al. [32] and Yoo et al. [61], who found that the adhesion strength strongly depends on the physical and the chemical interactions between the particles and the binder with the substrate. In this context, a paramount impact was attributed to the mechanical strength of the emerging polymer matrix [45]. Hence, an increase in the binder content leads to more interaction opportunities between the binder and the substrate and likely enhances the polymer matrix. Haselrieder et al. [45] postulated that the adhesion strength increases linearly with the molecular weight of the employed binder, apparently at the expense of the cohesion behavior. This was attributed to the weaker tendency of long-chain polymers to migrate and segregate upon drying. As a result, a more homogeneous distribution along the substrate is present, which causes a polymer matrix with a higher cross-linking. Consequently, the findings corroborate that the presence of the h-mw CMC favorably increases the adhesion strength, while it negatively affects the cohesion behavior.

### 3.3.2. Electrochemical Characteristics

**Voltage profiles.** The low mass of the coating samples leads to measurement inconsistencies and causes deviations in the calculated theoretical capacity values. To allow for a comparative analysis of the voltage profiles, the experimental times were standardized for each half-cell sample. Considering Figure 5, it is apparent that the l-mw and h-mw half-cell samples show similar curve characteristics. Each voltage curve exhibits an initially high voltage in the range between approx. 2.0 and 3.0 V (l-mw) and between 2.5 and 3.0 V (h-mw), which declines at a varying gradient. With increasing time, the voltage curves align with each other more accurately for each charge and discharge. Additionally, the discharge voltage curves become less drawn out after the first cycle. No clear differentiating trends can be identified that indicate a dependence of the voltage curves on the binder content. A direct comparison of representative half-cell samples (see Figure 6) elucidates that the l-mw half-cell sample shows shorter charge and discharge times than their h-mw counterpart.

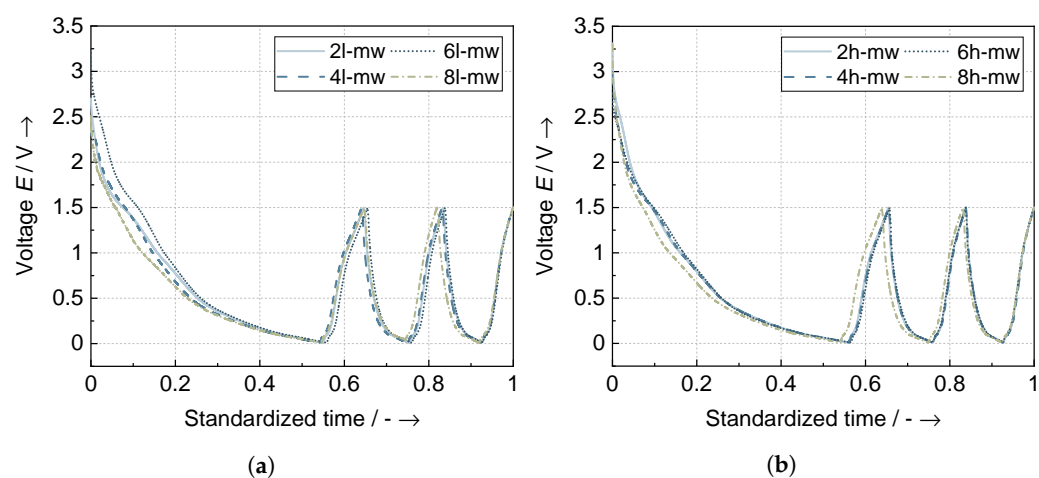


**Figure 5.** Voltage profiles of selected (a) l-mw and (b) h-mw half-cell samples.

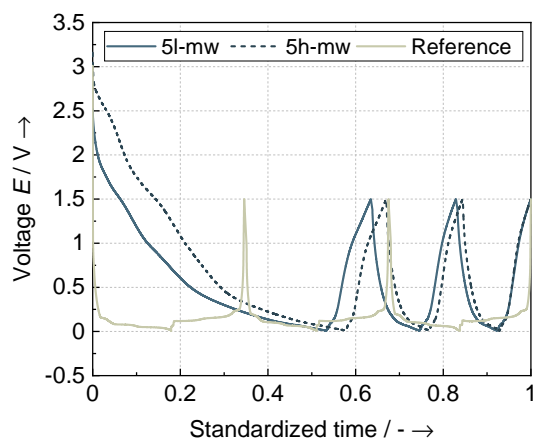


**Figure 6.** Comparison of the voltage profiles of a selected l-mw and h-mw half-cell sample and the reference half-cell.

The extensive first voltage decline into the set voltage boundaries of 0.01 and 1.50 V can be attributed to the initial formation of the solid electrolyte interphase (SEI) [62]. Upon the first discharge, the bulk of the SEI has already been generated, although a certain number of lithium ions are still utilized for the SEI formation. This also implies that the amount of lithium ions that can intercalate directly into the graphite host structure is larger, causing a more rapid decrease in the voltage values. The longer charge and discharge times of the h-mw half-cell samples can be attributed to the sterically more demanding nature of the h-mw CMC molecules. As the chain length increases, the accessibility to the graphite nanoparticle surface decreases. Therefore, the lithium ion pathways likely become more

extensive. Once the lithium ions have successfully made contact with the nanoparticles, the SEI is first formed before further intercalation can occur to neutralize the present charges. This also postpones the approach to 0.01 V.

Considering the voltage profile of the representative half-cell samples against the reference half-cell (see Figure 6) reveals a noticeably different discharge behavior. These deviations become particularly apparent during the first discharges. While the depicted reference half-cell is fully discharged at a standardized time stamp of 0.18, the 5l-mw and 5h-mw half-cell samples require time values of 0.53 and 0.58, respectively. This indicates more extensive SEI generation, which is ascribed to the significantly larger total surface area of the nanoscale graphite particles compared to the macrometer-sized reference graphite particles. Examining the BET surface area of the two materials unveils that the nanosized type (BET:  $195 \text{ m}^2 \text{ g}^{-1}$ ) exhibits a BET approx. 72 times larger than the conventional counterpart (BET:  $2.7 \text{ m}^2 \text{ g}^{-1}$ ). The deviance in the peak structure suggests that, unlike for the reference half-cell, the SEI is not yet fully formed for the l-mw and h-mw half-cell samples. Furthermore, the shape of the cycling curves differs significantly. This is indicative of a distinctly different characteristic active material behavior, which is further examined along with the capacity profiles.

**Capacity profiles.** The capacity profiles of the first cycle (see Figure 7) reflect the substantial initial capacity loss that was observed in the voltage profiles (see Figure 5). The curves signify the extent of the capacity losses which exceed 80% of the initial capacity for both derivatives. A clear correlation between the binder amount and its derivative and the associated capacity losses is not indicative in this depiction. However, the curves suggest that the l-mw half-cell samples exhibit a faster voltage drop during discharge. A direct comparison of representative half-cell samples (see Figure 8) confirms this observation and also verifies that the losses are slightly more distinct for the h-mw samples.

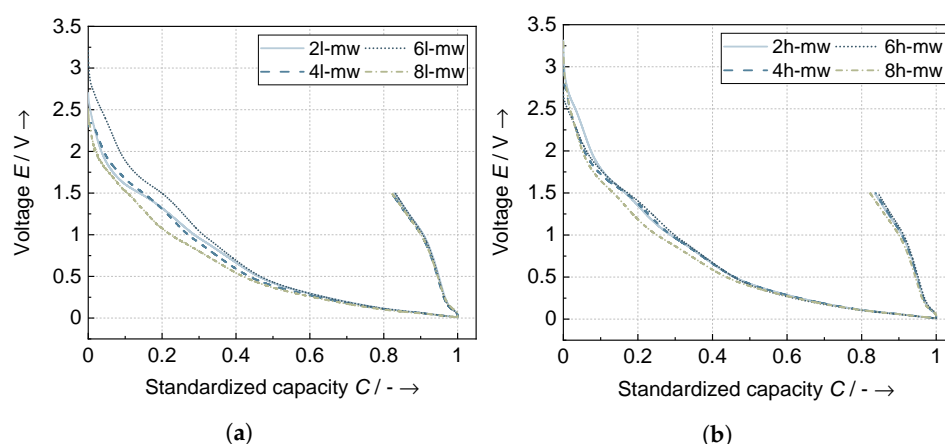


**Figure 7.** Capacity profiles of selected (a) l-mw and (b) h-mw half-cell samples.

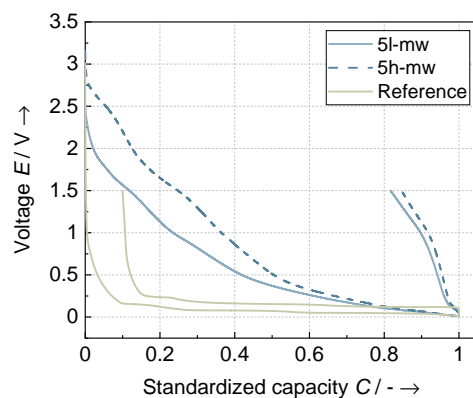


**Figure 8.** Comparison of the capacity profiles of a selected l-mw and h-mw half-cell sample and the reference half-cell.

The benchmark of the l-mw and h-mw half-cell samples against the reference half-cell (see Figure 7) corroborates the varying material behavior already indicated by the voltage profiles. While the voltage curve progression of the l-mw and the h-mw half-cell samples resembles a typical hard carbon behavior, the reference half-cell mirrors the performance of a characteristic graphitic material [63]. This is evidenced by the large irreversible capacities and the pronounced hysteresis between charge and discharge.

**Coulombic efficiencies.** The massive irreversible capacity losses are also reflected in the coulombic efficiencies (see Figure 9a). Overall, it appears that the l-mw half-cell samples tend to have larger *CE* values than their h-mw counterparts. This correlates with the observation made for the voltage profiles that the stronger shielding of the graphite particles owing to the longer chain lengths increases the ionic resistance. By analyzing the evolution of the coulombic efficiencies in the subsequent cycles (see Figure 9b), it can be observed that the *CE* improves significantly. The largest increase occurs between the first and the second cycle. This corroborates the assumption that the bulk of the SEI is generated in the first formation cycle, although a minor fraction of lithium ions are still expended for further SEI growth in the subsequent cycles.

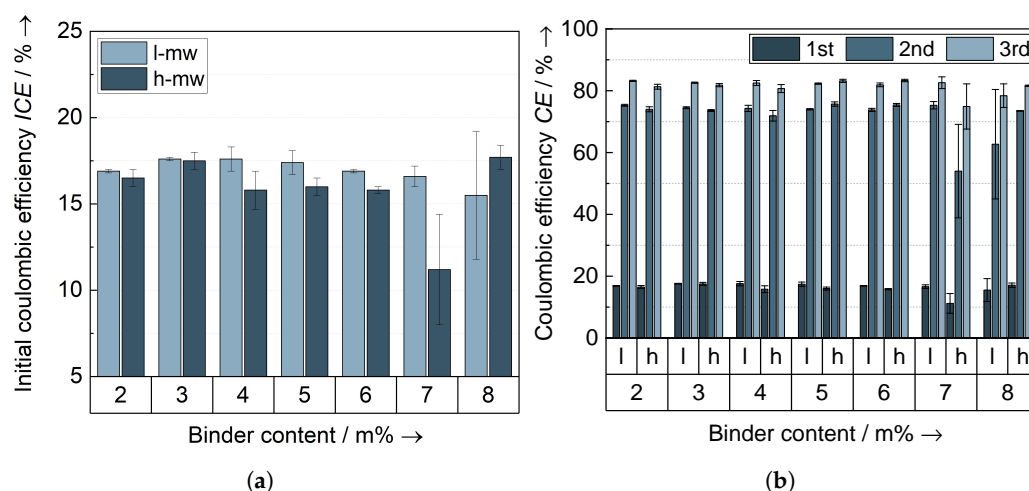


**Figure 9.** Evolution of the coulombic efficiencies with (a) initial coulombic efficiency *ICE* and (b) coulombic efficiency *CE* over the first three cycles; 1st, 2nd, and 3rd denote the first, the second, and the third cycle. l represents the l-mw and h the h-mw samples.

The comparative analysis with the reference half-cell (see Figure 10) elucidates a large discrepancy in the *CE* values. The reference half-cell exhibits an initial *CE* of roughly 90% and approximates 100% within the second and third cycle. The l-mw and h-mw half-cell samples, however, show an initial *CE* lower than 20%. Although the *CE* improves over the subsequent cycles, the values do not reach the ones of the reference half-cell. This reiterates that further cycles are required to attain a stable state after SEI formation and thus to approach the maximum *CE*. Furthermore, the *CE* provides information about the total irreversible capacity loss. While the reference half-cells lose only 10% of the initial capacity, it drops by more than 80% for the l-mw and h-mw half-cell samples. This is attributed to the different active material content, the strongly varying BET surface, and the differing material behavior [62].

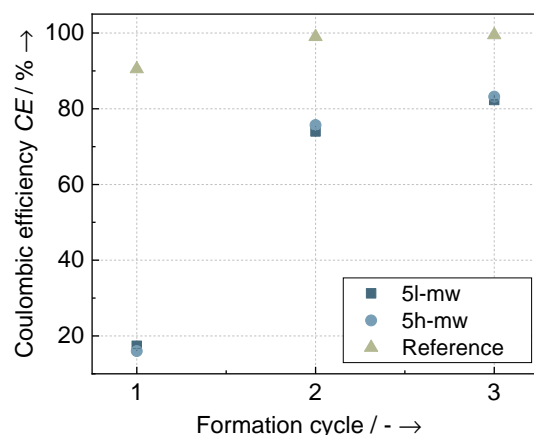


**Figure 10.** Comparison of the coulombic efficiency  $CE$  of a selected l-mw and h-mw half-cell sample and the reference half-cell.

#### 4. Conclusions

This paper examines the role of binder derivatives for aqueous graphite dispersions that were designed for use in inkjet printing. The impact on both the processability and the electrode characteristics was investigated. Two different CMC derivatives with strongly varying molecular weights were studied. The major results of this paper are condensed in Table 7.

**Table 7.** Comparison of the effects of the investigated CMC derivatives on the processability and the electrode characteristics; x indicates a comparatively more pronounced suitability.

Characteristic	l-mw	h-mw
<b>Processability</b>		
Drop formation	x	
Drop deposition	x	
<b>Electrode characteristics</b>		
Adhesion behavior		x
Cohesion behavior	x	
Electrochemical characteristics	x	

The findings demonstrate that the l-mw CMC affects most of the studied characteristics more favorably than the h-mw CMC. This proves the crucial function of binders for the successful production and operation of lithium-ion batteries. Furthermore, this testifies to the decisive importance of the appropriate selection of particular binder derivatives.

Based on the findings, a more extensive study with additional binder derivatives is pursued to directly correlate the inherent binder characteristics with the features investigated at the dispersion, electrode, and cell level. Future research will be concerned with the in-depth interactions between the key dispersion constituents to further increase the processable graphite content. Additionally, the results provide a motivation for a more extensive investigation of the leveraging effect of binder derivatives on conventional industrial lithium-ion battery production. Further research is required to assess the transferability of the results and their extent to traditional production methods. Apart from binders, further effort is required to develop nano-sized graphitic materials that are interphase-engineered to reduce the initial capacity losses.

**Author Contributions:** Conceptualization, C.G.K.; Investigation, C.G.K., A.S. and C.-M.T.; Data curation: C.G.K., A.S. and C.-M.T.; Funding acquisition, M.F.Z.; Methodology, C.G.K. and A.S.; Visualization, C.G.K. and C.-M.T.; Writing—original draft, C.G.K.; Writing—review and editing, M.L., H.P., S.M. and M.F.Z. All authors have read and agreed to the published version of the manuscript.

**Funding:** We express our sincere gratitude to the Federal Ministry of Education and Research (BMBF) for financially supporting the research on the presented topic within the research cluster ExZellTUM III (grant number 03XPO255).

**Institutional Review Board Statement:** Not applicable.

**Informed Consent Statement:** Not applicable.

**Data Availability Statement:** The data presented in this study are available on request from the corresponding author. The data are not publicly available due to its large file size.

**Acknowledgments:** We would like to thank Hanh My Bui (Department of Chemistry, Technical University of Munich) for the possibility of conducting contact angle measurements.

**Conflicts of Interest:** The authors declare that they have no known competing financial interests or personal relationships that could have appeared to influence the work reported in this paper.

## References

1. Hawes, G.; Rehman, S.; Rangom, Y.; Pope, M. Advanced manufacturing approaches for electrochemical energy storage devices. *Int. Mater. Rev.* **2023**, *68*, 323–364. [\[CrossRef\]](#)
2. Chang, P.; Mei, H.; Zhou, S.; Dassios, K.; Cheng, L. 3D printed electrochemical energy storage devices. *J. Mater. Chem.* **2019**, *7*, 4230–4258. [\[CrossRef\]](#)
3. Kwade, A.; Haselrieder, W.; Leithoff, R.; Modlinger, A.; Dietrich, F.; Droeder, K. Current status and challenges for automotive battery production technologies. *Nat. Energy* **2018**, *3*, 290–300. [\[CrossRef\]](#)
4. Zhang, F.; Wei, M.; Viswanathan, V.; Swart, B.; Shao, Y.; Wu, G.; Zhou, C. 3D printing technologies for electrochemical energy storage. *Nano Energy* **2017**, *40*, 418–431. [\[CrossRef\]](#)
5. Hawley, W.B.; Li, J. Electrode manufacturing for lithium-ion batteries—Analysis of current and next generation processing. *J. Energy Storage* **2019**, *25*, 100862. [\[CrossRef\]](#)
6. Lenze, G.; Bockholt, H.; Schilcher, C.; Froböse, L.; Jansen, D.; Krewer, U.; Kwade, A. Impacts of variations in manufacturing parameters on performance of lithium-ion-batteries. *J. Electrochem. Soc.* **2018**, *165*, A314. [\[CrossRef\]](#)
7. Zhu, C.; Liu, T.; Qian, F.; Chen, W.; Chandrasekaran, S.; Yao, B.; Song, Y.; Duoss, E.; Kuntz, J.; Spadaccini, C.; et al. 3D printed functional nanomaterials for electrochemical energy storage. *Nano Today* **2017**, *15*, 107–120. [\[CrossRef\]](#)
8. Yang, Y.; Yuan, W.; Zhang, X.; Yuan, Y.; Wang, C.; Ye, Y.; Huang, Y.; Qiu, Z.; Tang, Y. Overview on the applications of three-dimensional printing for rechargeable lithium-ion batteries. *Appl. Energy* **2020**, *257*, 114002. [\[CrossRef\]](#)
9. Lanceros-Méndez, S.; Costa, C.M. *Printed Batteries: Materials, Technologies and Applications*; John Wiley & Sons: Hoboken, NJ, USA, 2018.
10. Beuth. *ISO/ASTM 52900:2021; Additive Manufacturing—General Principles—Fundamentals and Vocabulary*. Beuth: Berlin, Germany, 2022.
11. Wijshoff, H. The dynamics of the piezo inkjet printhead operation. *Phys. Rep.* **2010**, *491*, 77–177. [\[CrossRef\]](#)
12. Kolb, C.; Lehmann, M.; Kriegler, J.; Lindemann, J.-L.; Bachmann, A.; Zaeh, M. Qualifying water-based electrode dispersions for the inkjet printing process: A requirements analysis. *Rapid Prototyp. J.* **2022**, *28*, 33–50. [\[CrossRef\]](#)
13. Derby, B.; Reis, N. Inkjet printing of highly particulate suspensions. *MRS Bull.* **2003**, *28*, 815–818. [\[CrossRef\]](#)
14. Gu, Y.; Wu, A.; Sohn, H.; Nicoletti, C.; Iqbal, Z.; Federici, J. Fabrication of rechargeable lithium ion batteries using water-based inkjet printed cathodes. *J. Manuf. Process* **2015**, *20*, 198–205. [\[CrossRef\]](#)
15. Clasen, C.; Philipps, P.; Palangetic, L.; Vermant, A. Dispensing of rheologically complex fluids: The map of misery. *AIChE J.* **2012**, *58*, 3242–3255. [\[CrossRef\]](#)
16. Lestriez, B. Functions of polymers in composite electrodes of lithium ion batteries. *Comptes Rendus Chim.* **2010**, *13*, 1341–1350. [\[CrossRef\]](#)
17. Bresser, D.; Buchholz, D.; Moretti, A.; Varzi, A.; Passerini, S. Alternative binders for sustainable electrochemical energy storage—The transition to aqueous electrode processing and bio-derived polymers. *Energy Environ. Sci.* **2018**, *11*, 3096–3127. [\[CrossRef\]](#)
18. Costa, C.; Lizundia, E.; Lanceros-Mendez, S. Polymers for advanced lithium-ion batteries: State of the art and future needs on polymers for the different battery components. *Prog. Energy Combust. Sci.* **2020**, *79*, 100846. [\[CrossRef\]](#)
19. Arora, P.; White, R.E.; Doyle, M. Capacity fade mechanisms and side reactions in lithium-ion batteries. *J. Electrochem. Soc.* **1998**, *145*, 3647. [\[CrossRef\]](#)
20. Rahani, E.K.; Shenoy, V.B. Role of plastic deformation of binder on stress evolution during charging and discharging in lithium-ion battery negative electrodes. *J. Electrochem. Soc.* **2013**, *160*, A1153. [\[CrossRef\]](#)
21. Porcher, W.; Moreau, P.; Lestriez, B.; Jouanneau, S.; Le Cras, F.; Guyomard, D. Stability of LiFePO<sub>4</sub> in water and consequence on the Li battery behaviour. *Ionics* **2008**, *14*, 583–587. [\[CrossRef\]](#)
22. Buchdahl, R.; Thimm, J. The relationship between the rheological properties and working properties of printing inks. *J. Appl. Phys.* **1945**, *16*, 344–350. [\[CrossRef\]](#)

23. Xu, D.; Sanchez-Romaguera, V.; Barbosa, S.; Travis, W.; de Wit, J.; Swan, P.; Yeates, S. Inkjet printing of polymer solutions and the role of chain entanglement. *J. Mater. Chem.* **2007**, *17*, 4902–4907. [[CrossRef](#)]
24. Shore, H.J.; Harrison, G.M. The effect of added polymers on the formation of drops ejected from a nozzle. *Phys. Fluids* **2005**, *17*, 033104. [[CrossRef](#)]
25. Bergstrom, L. Colloidal processing of ceramics. *Handb. Appl. Surf. Colloid Chem.* **2001**, *1*, 201–217.
26. Jianping, L.; Guiling, D. Technology development and basic theory study of fluid dispensing-A review. In Proceedings of the Sixth IEEE CPMT Conference on High Density Microsystem Design and Packaging and Component Failure Analysis (HDP'04), Shanghai, China, 3–4 July 2004; pp. 198–205.
27. Chou, S.L.; Wang, J.Z.; Liu, H.K.; Dou, S.X. Rapid synthesis of  $\text{Li}_4\text{Ti}_5\text{O}_{12}$  microspheres as anode materials and its binder effect for lithium-ion battery. *J. Phys. Chem. C* **2011**, *115*, 16220–16227. [[CrossRef](#)]
28. Lee, B.R.; Oh, E.S. Effect of molecular weight and degree of substitution of a sodium-carboxymethyl cellulose binder on  $\text{Li}_4\text{Ti}_5\text{O}_{12}$  anodic performance. *J. Phys. Chem. C* **2013**, *117*, 4404–4409. [[CrossRef](#)]
29. Park, Y.S.; Oh, E.S.; Lee, S.M. Effect of polymeric binder type on the thermal stability and tolerance to roll-pressing of spherical natural graphite anodes for Li-ion batteries. *J. Power Sources* **2014**, *248*, 1191–1196. [[CrossRef](#)]
30. Li, J.; Lewis, R.; Dahn, J. Sodium carboxymethyl cellulose: A potential binder for Si negative electrodes for Li-ion batteries. *Electrochem. Solid State Lett.* **2006**, *10*, A17. [[CrossRef](#)]
31. Lingappan, N.; Kong, L.; Pecht, M. The significance of aqueous binders in lithium-ion batteries. *Renew. Sustain. Energy Rev.* **2021**, *147*, 111227. [[CrossRef](#)]
32. Liu, W.R.; Yang, M.H.; Wu, H.C.; Chiao, S.; Wu, N.L. Enhanced cycle life of Si anode for Li-ion batteries by using modified elastomeric binder. *Electrochem. Solid State Lett.* **2004**, *8*, A100. [[CrossRef](#)]
33. Lee, J.H.; Paik, U.; Hackley, V.A.; Choi, Y.M. Effect of carboxymethyl cellulose on aqueous processing of natural graphite negative electrodes and their electrochemical performance for lithium batteries. *J. Electrochem. Soc.* **2005**, *152*, A1763. [[CrossRef](#)]
34. Kolb, C.G.; Lehmann, M.; Teixeira, C.M.; Maleksaeedi, S.; Zaeh, M.F. A priori evaluation of the printability of water-based anode dispersions in inkjet jetting. *PIAM 2023, Submitted*. [[CrossRef](#)]
35. Kolb, C.; Lehmann, M.; Lindemann, J.; Bachmann, A.; Zaeh, M. Improving the Dispersion Behavior of Organic Components in Water-Based Electrode Dispersions for Inkjet Printing Processes. *Appl. Sci.* **2021**, *11*, 2242. [[CrossRef](#)]
36. Kolb, C.; Lehmann, M.; Kulmer, D.; Zaeh, M. Modeling of the stability of water-based graphite dispersions using polyvinylpyrrolidone on the basis of the DLVO theory. *Heliyon* **2022**, *8*, 11988. [[CrossRef](#)]
37. Wuestenberg, T. *Cellulose and Cellulose Derivatives in the Food Industry: Fundamentals and Applications*; John Wiley & Sons: Hoboken, NJ, USA, 2014.
38. Mark, H.F. *Encyclopedia of Polymer Science and Technology, Concise*; John Wiley & Sons: Hoboken, NJ, USA, 2013.
39. Lee, J.H.; Lee, S.; Paik, U.; Choi, Y.M. Aqueous processing of natural graphite particulates for lithium-ion battery anodes and their electrochemical performance. *J. Power Sources* **2005**, *147*, 249–255. [[CrossRef](#)]
40. Ishii, M.; Nakamura, H. Influence of molecular weight and concentration of carboxymethyl cellulose on rheological properties of concentrated anode slurries for lithium-ion batteries. *JCIS Open* **2022**, *6*, 100048. [[CrossRef](#)]
41. He, B.; Yang, S.; Qin, Z.; Wen, B.; Zhang, C. The roles of wettability and surface tension in droplet formation during inkjet printing. *Sci. Rep.* **2017**, *7*, 11841. [[CrossRef](#)]
42. Tadros, T. *Rheology of Dispersions: Principles and Applications*; John Wiley & Sons: Hoboken, NJ, USA, 2011.
43. Herschel, W.; Bulkley, R. Konsistenzmessungen von Gummi-Benzollösungen. *Kolloid Z.* **1926**, *39*, 291–300. [[CrossRef](#)]
44. Traube, J. Über die Capillaritätsconstanten organischer Stoffe in wässrigen Lösungen. *Justus Liebigs Ann. Chem.* **1891**, *265*, 27–55. [[CrossRef](#)]
45. Haselrieder, W.; Westphal, B.; Bockholt, H.; Diener, A.; Höft, S.; Kwade, A. Measuring the coating adhesion strength of electrodes for lithium-ion batteries. *Int. J. Adhes. Adhes.* **2015**, *60*, 1–8. [[CrossRef](#)]
46. Lehmann, M.; Kolb, C.G.; Klinger, F.; Zaeh, M.F. Preparation, characterization, and monitoring of an aqueous graphite ink for use in binder jetting. *Mater. Des.* **2021**, *207*, 109871. [[CrossRef](#)]
47. Barnes, H. *A Handbook of Elementary Rheology*; University of Wales, Institute of Non-Newtonian Fluid Mechanics: Wales, UK, 2000.
48. Delannoy, P.; Riou, B.; Brousse, T.; Le Bideau, J. Ink-jet printed porous composite  $\text{LiFePO}_4$  electrode from aqueous suspension for microbatteries. *J. Power Sources* **2015**, *287*, 261–268. [[CrossRef](#)]
49. Mezger, T.G. *The Rheology Handbook: For Users of Rotational and Oscillatory Rheometers*; Vincentz Network: Hanover, Germany, 2016.
50. Hoath, S. *Fundamentals of Inkjet Printing: The Science of Inkjet and Droplets*; John Wiley & Sons: Hoboken, NJ, USA, 2016.
51. Jeschull, F.; Brandell, D.; Wohlfahrt-Mehrens, M.; Memm, M. Water-soluble binders for lithium-ion battery graphite electrodes: slurry rheology, coating adhesion, and electrochemical performance. *Energy Technol.* **2017**, *5*, 2108–2118. [[CrossRef](#)]
52. Guy, B.; Hermes, M.; Poon, W.C. Towards a unified description of the rheology of hard-particle suspensions. *Phys. Rev. Lett.* **2015**, *115*, 088304. [[CrossRef](#)]
53. Mari, R.; Seto, R.; Morris, J.F.; Denn, M.M. Shear thickening, frictionless and frictional rheologies in non-Brownian suspensions. *J. Rheol.* **2014**, *58*, 1693–1724. [[CrossRef](#)]
54. Jang, D.; Kim, D.; Moon, J. Influence of fluid physical properties on ink-jet printability. *Langmuir* **2009**, *25*, 2629–2635. [[CrossRef](#)]
55. Morrison, N.F.; Harlen, O.G. Viscoelasticity in inkjet printing. *Rheol. Acta* **2010**, *49*, 619–632. [[CrossRef](#)]

56. Wenzel, V.; Nirschl, H.; Nötzel, D. Challenges in lithium-ion-battery slurry preparation and potential of modifying electrode structures by different mixing processes. *Energy Technol.* **2015**, *3*, 692–698. [[CrossRef](#)]
57. Ryan, B.; Poduska, K. Roughness effects on contact angle measurements. *Am. J. Phys.* **2008**, *76*, 1074–1077. [[CrossRef](#)]
58. Saulick, Y.; Lourenco, S.; Baudet, B. A semi-automated technique for repeatable and reproducible contact angle measurements in granular materials using the sessile drop method. *Soil Sci. Soc. Am. J.* **2017**, *81*, 241–249. [[CrossRef](#)]
59. Vuckovac, M.; Latikka, M.; Liu, K.; Huhtamäki, T.; Ras, R. Uncertainties in contact angle goniometry. *Soft Matter* **2019**, *15*, 7089–7096. [[CrossRef](#)]
60. Billot, N.; Beyer, M.; Koch, N.; Ihle, C.; Reinhart, G. Development of an adhesion model for graphite-based lithium-ion battery anodes. *J. Manuf. Syst.* **2021**, *58*, 131. [[CrossRef](#)]
61. Yoo, M.; Frank, C.W.; Mori, S.; Yamaguchi, S. Effect of poly (vinylidene fluoride) binder crystallinity and graphite structure on the mechanical strength of the composite anode in a lithium ion battery. *Polymer* **2003**, *44*, 4197–4204. [[CrossRef](#)]
62. Winter, M.; Novák, P.; Monnier, A. Graphites for lithium-ion cells: The correlation of the first-cycle charge loss with the brunauer-emmett-teller surface area. *J. Electrochem. Soc.* **1998**, *145*, 428. [[CrossRef](#)]
63. Buiel, E.; Dahn, J. Li-insertion in hard carbon anode materials for Li-ion batteries. *Electrochim. Acta* **1999**, *45*, 121–130. [[CrossRef](#)]

**Disclaimer/Publisher's Note:** The statements, opinions and data contained in all publications are solely those of the individual author(s) and contributor(s) and not of MDPI and/or the editor(s). MDPI and/or the editor(s) disclaim responsibility for any injury to people or property resulting from any ideas, methods, instructions or products referred to in the content.